

Thermal Analysis of the Anti-Submarine Penetrator Surface Pressure Transducers

Douglas N. Benton
Aerothermodynamics Division
Sandia National Laboratories
Albuquerque, NM 87185

Abstract

Analysis of the Anti-Submarine Penetrator aerothermodynamic environment showed that the surface pressure transducers mounted in the vehicle case required thermal protection. Recessing the transducers below the case surface and covering them with a 0.050-in. layer of RTV compound provided sufficient thermal protection but reduced transducer frequency response and repeatability. Mounting the transducers at the bottom of open cavities below the vehicle surface also proved unacceptable. The large cavity depth to cavity diameter ratio required to sufficiently lower heat transfer to the transducer, a value of about 26, unacceptably reduced transducer frequency response. The final solution consisted of filling the open cavity, having a depth of 0.070 in. and a diameter of 0.050 in., with a viscous silicone oil. The incompressible silicone oil does not significantly affect frequency response and insulates the transducer from the freestream environment.

Contents

1	Introduction	8
2	ASP Vehicle Description	8
3	Vehicle Trajectory	9
4	Pressure Instrumentation	10
5	Aerodynamic Heating Analysis	11
6	Indepth Conduction Analysis	11
6.1	Vehicle Case Conduction Analysis	13
6.2	Pressure Transducer Conduction Analysis	15
6.3	Subsurface Cavity Mounted Transducers	17
6.4	Silicone Oil Filled Cavity	18
6.5	Transducer Sensitivity to Transverse Temperature Gradients	18
7	Heat Transfer to the Bottom of a Cavity	21
8	Conclusion	24
9	References	25
A	Vehicle Trajectory	26
A.1	Computed Atmospheric Trajectory	27
A.2	Trajectory After Water Entry	29
B	Gap Heating Data Derived From Reference 11	30

List of Figures

1	ASP Vehicle	8
2	ASP Atmospheric Trajectory	9
3	ASP Trajectory After Water Entry	10
4	Computed ASP Heat Transfer Rates	12
5	Computed ASP Heat Transfer Rates at the 27.33-in. Station After Water Entry	13
6	Predicted ASP Case Temperatures at the 27.33-in. Station	14
7	Predicted ASP Case Temperatures at the 27.33-in. Station After Water Entry	15

8	Thermal Model and Predicted Pressure Transducer Temperature for the Transducer Mounted Flush With the Vehicle Surface	16
9	Cavity Mounted Pressure Transducer Configuration	17
10	Nestler, Saydah, and Auxer Gap Bottom Heating Correlation Plotted for End of Trajectory Conditions at the 27.33-in. Station	18
11	Thermal Model and Predicted Pressure Transducer Temperature Beneath a Cavity Filled with Silicone Oil	19
12	Thermal Model and Predicted Pressure Transducer Temperature Beneath a Duroid Washer	20
13	Nestler, Saydah, and Auxer Gap Bottom Heating Correlation	24

Nomenclature

H	cavity depth
k_d	thermal conductivity of air along the cavity dividing streamline
k_s	thermal conductivity of air at the vehicle surface
L	cavity diameter or length
M_e	boundary layer edge Mach number
q	compressible heat flux to flat plate
q_b	heat flux to the bottom of a cavity
q_c	heat flux crossing the dividing streamline into a cavity
q_i	incompressible heat flux to a flat plate
q_s	heat flux to the surface if the cavity were not present
Re_s	Reynolds number based on surface streamlength from the vehicle nosetip and boundary layer edge properties
T	temperature (deg R)
u_d	velocity along the cavity dividing streamline

Greek Symbols

δ	boundary layer thickness
δ^*	boundary layer displacement thickness
μ_d	viscosity of air along the dividing streamline
Φ	variable defined by Equation 3
σ	turbulent shear layer spread parameter

1 Introduction

The purpose of the Anti-Submarine Penetrator (ASP) Program is to develop a weapon capable of Arctic ice penetration or water entry without broaching. The test program for the RAP-200 series vehicle includes three instrumented flights from Kauai with a water entry. The instrumentation for these flights includes eight transducers which measure surface pressures after the water entry. The relatively low aerothermodynamic heating experienced by the vehicle poses no threat to the structural integrity of the vehicle. The pressure transducers, however, are only temperature compensated over a maximum range of 250 deg *R*. Since the water at depth is at a temperature of 520 deg *R*, the transducer temperature can not exceed 770 deg *R* without exceeding the compensation range. At the point in the trajectory where the vehicle reaches an altitude of 5177 ft and a Mach number of 2.37 the boundary layer recovery temperature is 973 deg *R*. Because of their low thermal capacity and isolation from the vehicle case, the temperature of pressure transducers mounted flush with the vehicle surface will be close to the boundary layer recovery temperature. This report discusses the analysis of the transducer aerothermal environment and the design of a thermal protection system to insulate the transducers from excessive heating.

2 ASP Vehicle Description

Figure 1 shows the ASP external configuration. The vehicle is a 64.92-in. long tangent ogive-cone with a 14.7-in. diameter base. The 20-caliber, 294-in. radius, ogive forebody is 32.32 in. long and begins with an approximately 0.10-in. radius spherical nose. At the 32.32-in. station, where the body diameter is 9.25 in., the ogive is tangent to a 4.78-degree half-angle conical frustum. The vehicle case is 0.25-in. thick 4340 steel and the forebody contains a tungsten alloy ballast. Overall weight of the vehicle is 770 lbs.

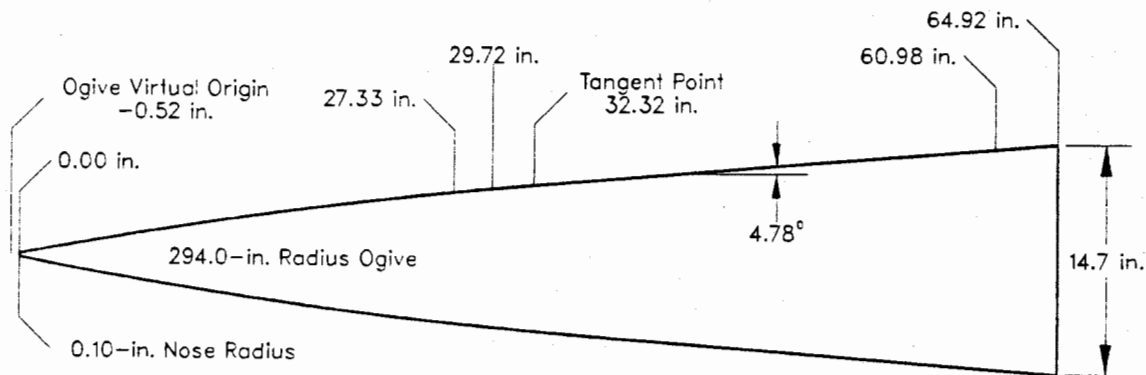


Figure 1: ASP Vehicle

3 Vehicle Trajectory

The ASP trajectory contains both an atmospheric portion and an underwater portion following water entry. Although the only significant heating occurs in the atmosphere, the underwater portion of the trajectory is included in the thermal analysis to estimate the rate at which the vehicle cools after water entry. Appendix A contains a listing of the computed atmospheric trajectory and the trajectory after water entry.

Figure 2 shows the atmospheric trajectory used for the heating analysis. The trajectory consists of powered flight for the first 3.5 seconds to a Mach number of 1.61 and an altitude of 1448 ft, followed by a ballistic cruise to an apogee at Mach 0.89 and an altitude of 6851 ft at 20.3 seconds. At 26.7 seconds into the flight, at Mach 0.85 and an altitude of 6200 ft, the second stage rocket burns for 2 seconds and accelerates the vehicle to Mach 2.37 at an altitude of 5177 ft. The final plunge into the water occurs at 36.7 seconds and a Mach number of 1.8.

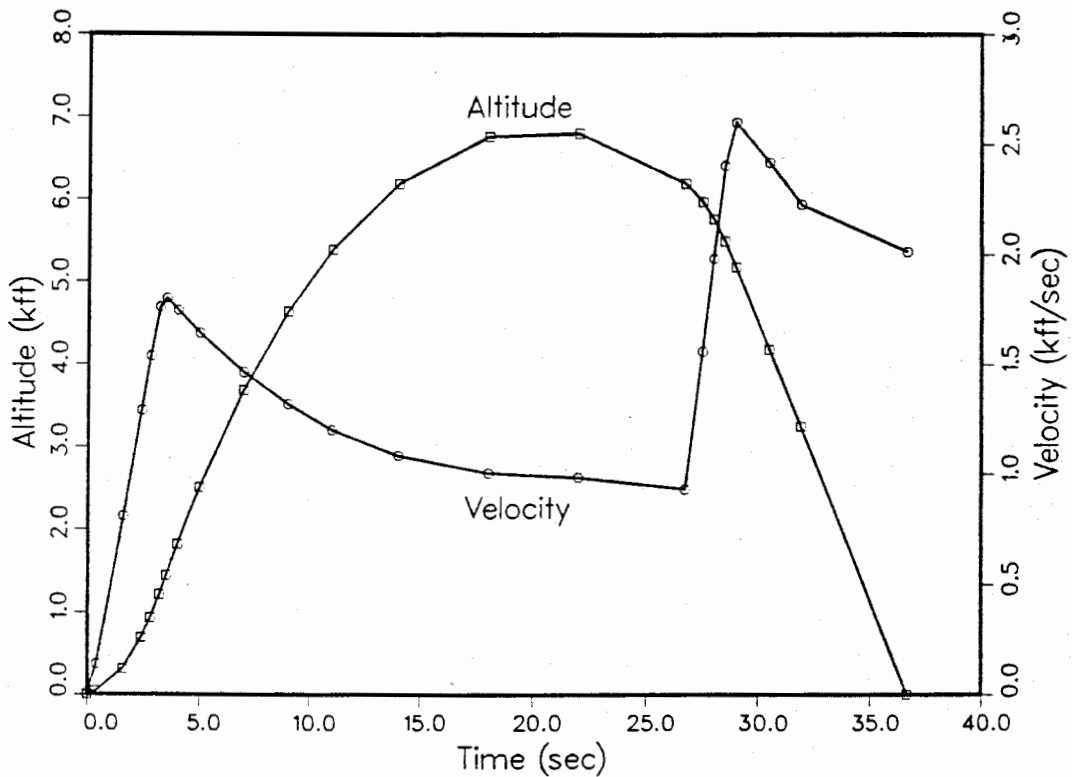


Figure 2: ASP Atmospheric Trajectory

Figure 3 shows the underwater trajectory of the vehicle after water entry at 2012 ft/sec. This trajectory represents a worst case scenario in that the vehicle's maximum water entry velocity is approximately 2000 ft/sec. After 1 second the vehicle has slowed to 105 ft/sec and reached a depth of 243 ft. After 6.8 seconds the vehicle has slowed to 45 ft/sec and reached the recovery system deployment depth of 500 ft. The water temperature varied from 542 deg R at the surface to 531 deg R at a depth of 500 ft.

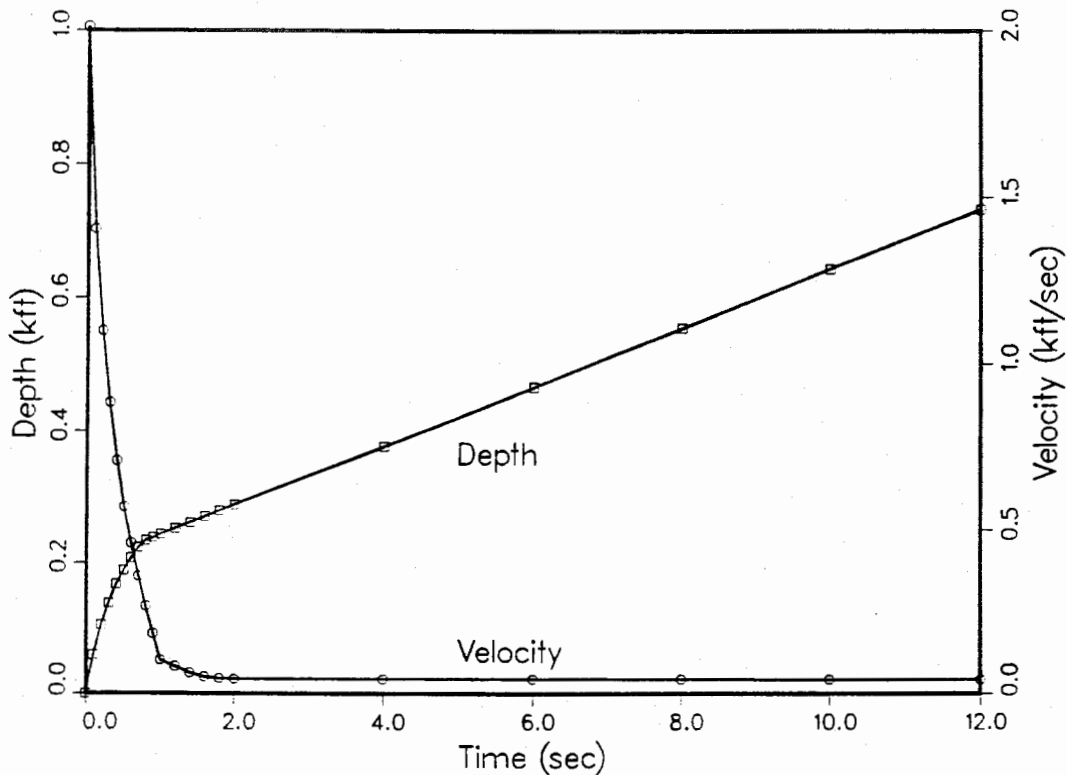


Figure 3: ASP Trajectory After Water Entry

4 Pressure Instrumentation

Transducer locations are measured along the vehicle axis from the nosetip. One pressure transducer is mounted at each of the axial locations 27.33 in. and 29.72 in. Four pressure transducers are mounted 60.98 in. from the vehicle nosetip. The remaining two transducers are mounted on the base of the vehicle. The transducer located at 27.33 in., where the surface pressure coefficient is unity when the vehicle is submerged, measures water depth pressure to obtain an independent depth measurement. The other seven transducers measure the low pressures existing in the cavities formed on the vehicle surface immediately after water entry. These cavities collapse quickly and the pressure transducer readings will then go off scale.

The pressure transducer assembly is 0.140 in. in diameter and 0.155 in. long. The sensing element of the depth pressure transducer consists of a thin silicon wafer 0.0017 in. thick. The other transducer sensing elements are 0.00045 in. thick silicon wafers. The sensing elements of all the transducers are covered by 0.010 in. of RTV topped with a 0.005-in. stainless steel screen exposed to the freestream pressure. Properties of RTV used in this analysis are those of Dow Corning 3145. The screen is assumed to have 50% porosity with the pores in the screen filled with RTV. Filling the screen pores with RTV eliminates the possibility of roughness augmented heating. The thermal properties of the screen are taken as the average of those of RTV and 304 stainless steel.

5 Aerodynamic Heating Analysis

The LOVEL low velocity aeroheating program [10] was used to predict the heating environment experienced by the vehicle. This program is useful for predicting heat transfer rates on vehicles at Mach numbers less than 6. The code predicts heating on simple shapes such as flat plates, sharp cones and sharp wedges, and sphere-cones and cylinder-wedges. It makes use of empirical heat transfer correlations, based on the distance from the vehicle nosetip, to calculate coldwall heat transfer rates. The coldwall heat transfer rate is referenced to an arbitrary wall temperature of 536 deg *R*.

To calculate the ASP aerodynamic heating, the vehicle was treated as two distinct sphere-cones. A tangent line to the ASP surface at the 27.33-in. station forms an angle of 5.7 degrees with the vehicle centerline. The forward section, therefore, was treated as a sphere-cone with body half-angle of 5.7 degrees. The rear station was treated as a sphere-cone with body half-angle of 4.7 degrees. Heat transfer calculations were made at the 27.33-in. and the 60.98-in. stations. Heating at the 29.72-in. station will be slightly less than heating at the 27.33-in. station. Turbulent flow was assumed for all of the calculations. The Reynolds number, based on streamwise distance from the nosetip and boundary layer edge properties, at the 27.33-in. station and the end of the vehicle trajectory is 30 million, well within the regime where turbulent flow is expected.

Figure 4 shows the predicted coldwall heat transfer rates at the vehicle nosetip, 27.33-in. station, and 60.98-in. station. The heating is highest at the nosetip and decreases as distance from the nosetip increases. Experimental results show that reentry vehicle base heating in hypersonic flow is an order of magnitude lower than side wall heating [4]. Although these results can not be extrapolated to the low supersonic Mach numbers of the ASP experiment, the base should see significantly lower heat transfer rates than the vehicle side wall.

To calculate the rate at which the vehicle cools upon entering the water, the NEPTUNE program was written using the sharp cone heat transfer relationships employed by LOVEL but with water properties. The program took advantage of the fact that at the 27.33-in. station the boundary layer edge pressure is the same as the freestream pressure after water entry. The boundary layer edge velocity, therefore, is the same as the freestream velocity. Figure 5 shows a plot of the coldwall heat transfer rate for the underwater portion of the trajectory at the 27.33-in. station.

6 Indepth Conduction Analysis

All of the conduction analysis was performed on one-dimensional models even when the nature of the problem justified a two-dimensional model. The one-dimensional solution always bracketed the effects of interest. The Charring Material Ablation (CMA) computer program [3] was used with heating input from LOVEL and NEPTUNE to calculate a one-dimensional indepth conduction solution. The CMA program uses a surface energy balance to couple the coldwall convective heat transfer prediction to the

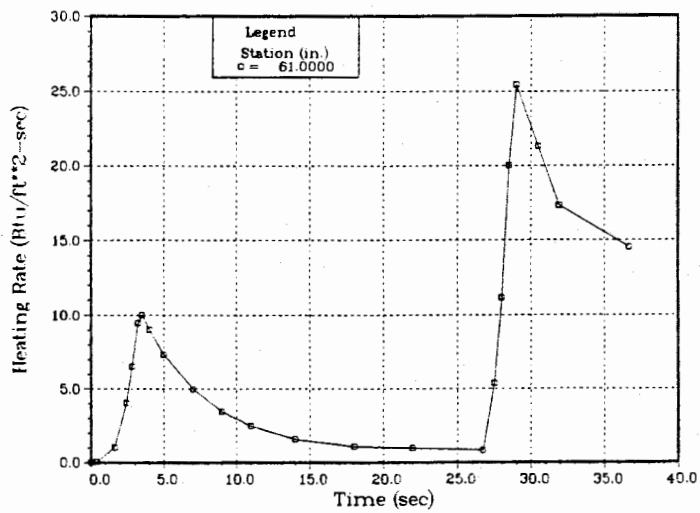
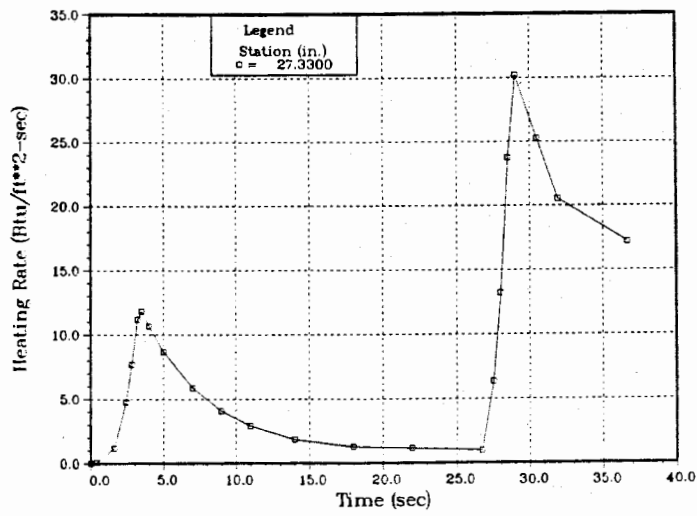
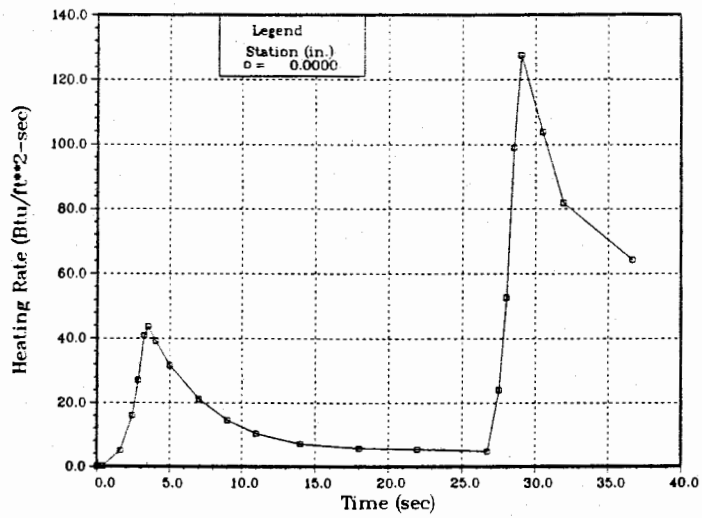


Figure 4: Computed ASP Heat Transfer Rates

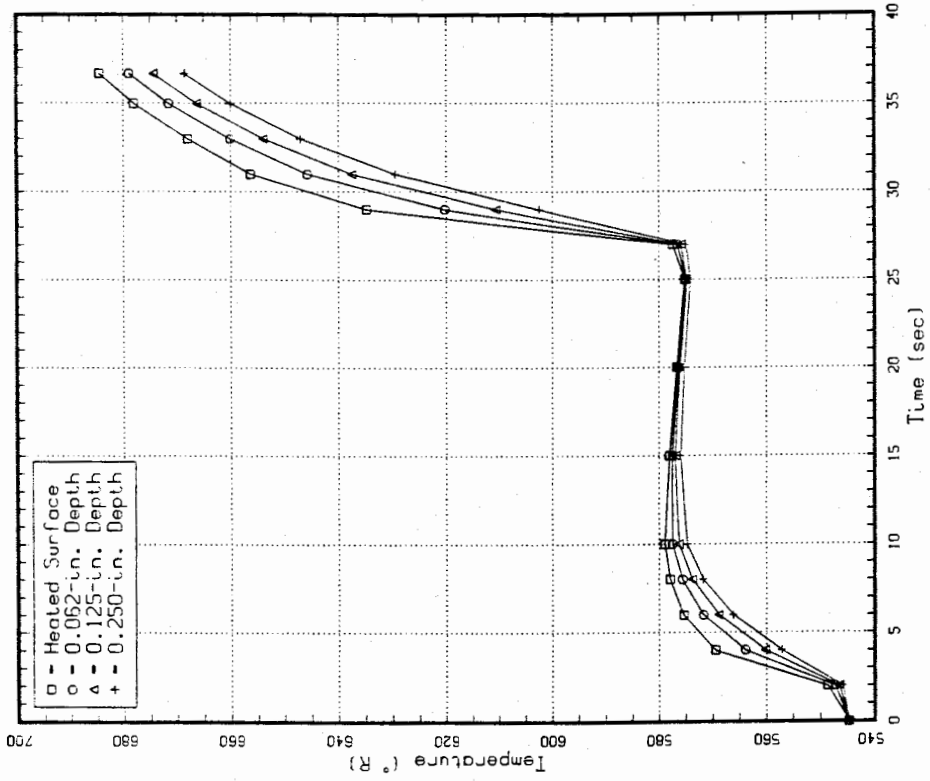
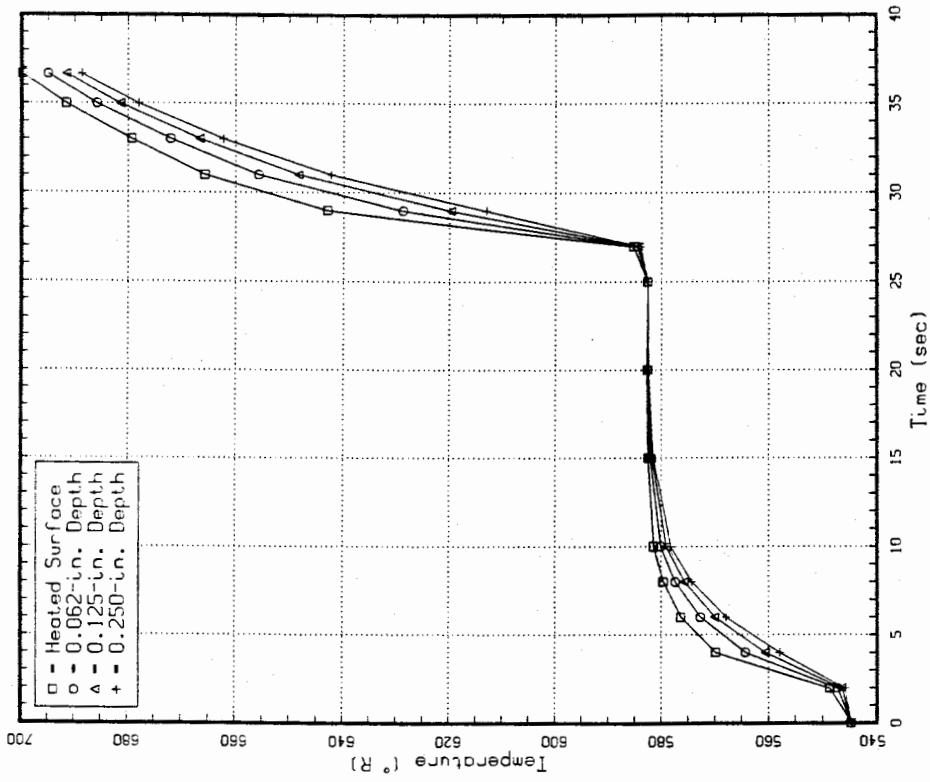
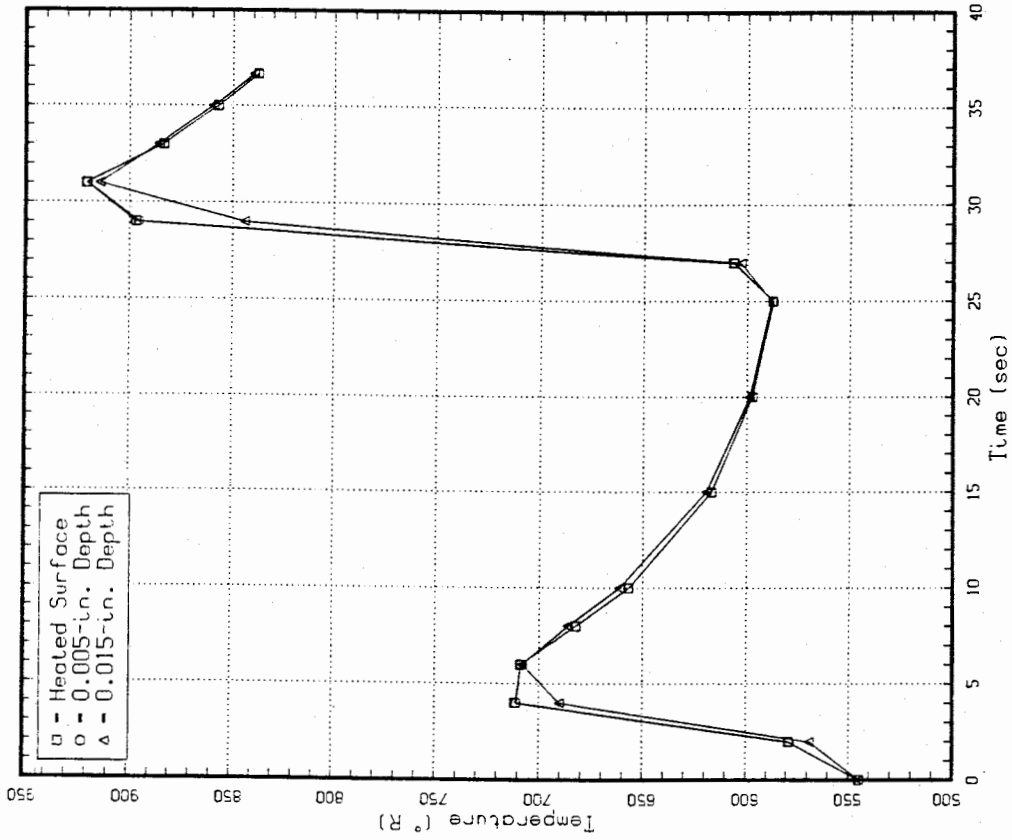


Figure 6: Predicted ASP Case Temperatures at the 27.33-in. Station



Freestream

0.005 in. Screen

0.010 in. RTV

0.0017 in. Silicon

Radiation to a Heat Sink at 544.7°R

Figure 8: Thermal Model and Predicted Pressure Transducer Temperature for the Transducer Mounted Flush With the Vehicle Surface

6.3 Subsurface Cavity Mounted Transducers

To shield the transducers from the freestream environment, mounting the transducers in cavities below the vehicle surface, as shown in Figure 9, was investigated. An analysis with CMA showed that the heat transfer rate to the pressure transducer, q_b , must be lowered by a factor of 20 relative to the heat transfer rate to a pressure transducer mounted on the vehicle surface at the same position, q_s . Because the 0.25-in. case thickness limits the cavity depth to 0.070 in., the problem became one of choosing the cavity diameter to insure a low heat transfer rate at the cavity bottom. The minimum ASP transducer cavity diameter is 0.050 in. Smaller diameters yield a cavity diameter to depth ratio, L/H , small enough to significantly attenuate the transducer frequency response.

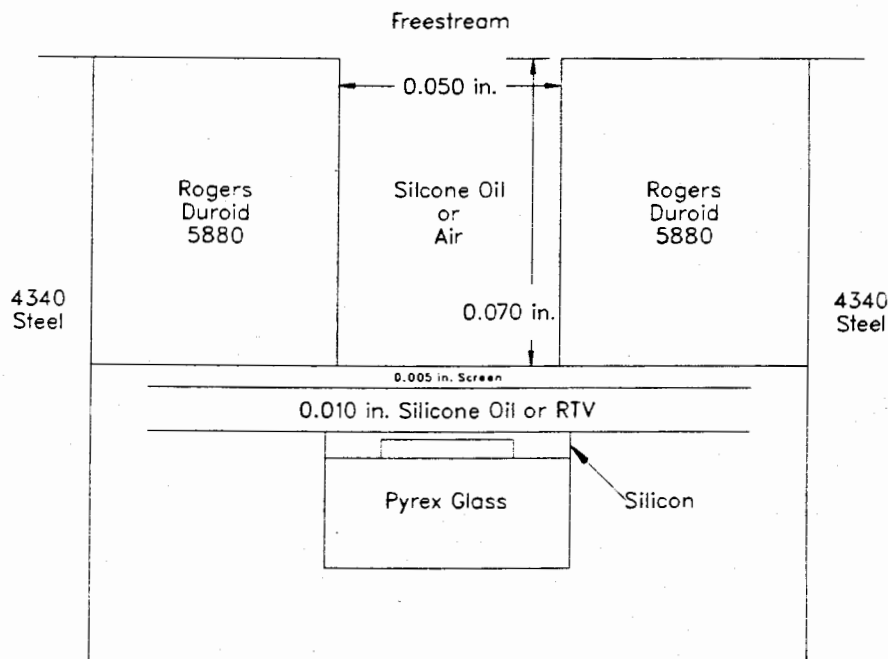


Figure 9: Cavity Mounted Pressure Transducer Configuration

Figure 10 shows q_b/q_s from a correlation developed by Nestler, Saydah, and Auxer [8] plotted versus H/L for conditions in the ASP vehicle boundary layer at the end of the air trajectory at the 27.33-in. station. Heat transfer to the bottom of cavities and the correlation plotted in Figure 10, are discussed more thoroughly later. Assuming that the correlation holds, Figure 10 shows that $H/L = 26$ is required to obtain $q_b/q_s = 0.05$. The maximum cavity depth of 0.070 in. and minimum cavity diameter of 0.050 in., or $H/L = 1.4$, yields $q_b/q_s = 0.68$. Transducer cavity depth limitations prevent use of this technique to protect the pressure transducers.

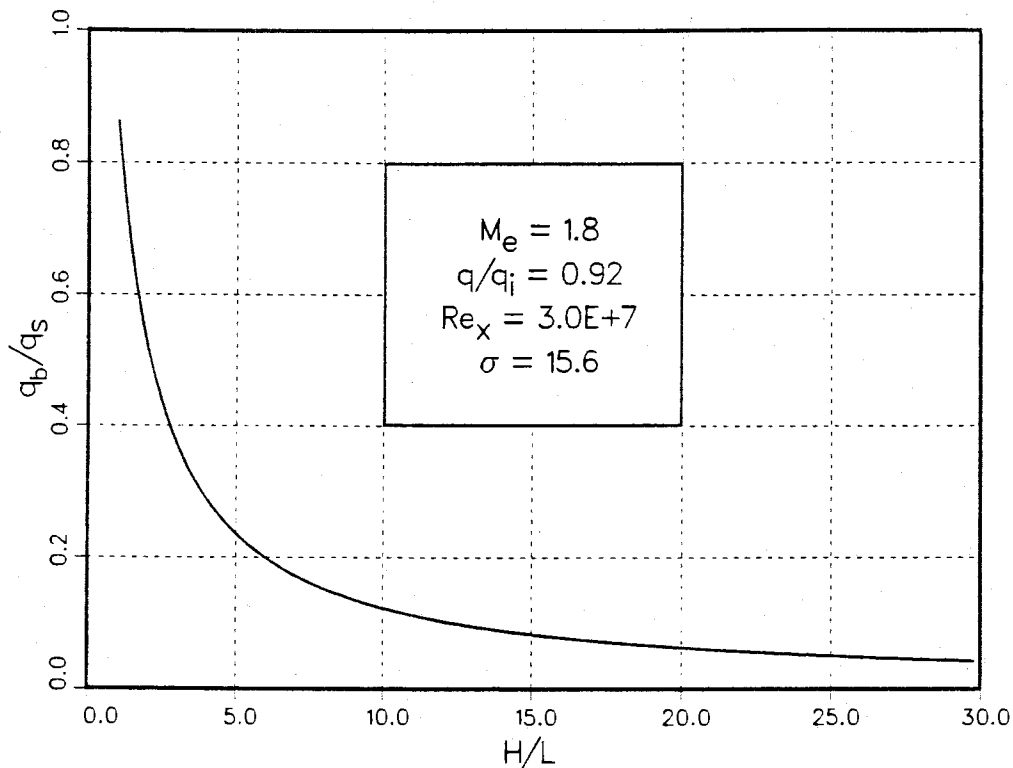


Figure 10: Nestler, Saydah, and Auxer Gap Bottom Heating Correlation Plotted for End of Trajectory Conditions at the 27.33-in. Station

6.4 Silicone Oil Filled Cavity

To overcome the limitations on the transducer cavity depth, the cavity will be filled with a viscous, essentially incompressible, silicone oil. This technique thermally insulates the pressure transducer and prevents any frequency response loss caused by the cavity. Because silicone oil causes RTV swelling, no RTV can be used in the transducer assembly. Therefore, the 0.010 in. of RTV seen in Figure 9 is replaced by silicone oil. Figure 11 shows the thermal model of the pressure transducer mounted below 0.071 in. of silicone oil and the results of the CMA conduction calculations. The transducer sees a maximum temperature of 636 deg *R*, well within the acceptable temperature range.

6.5 Transducer Sensitivity to Transverse Temperature Gradients

In addition to an absolute temperature sensitivity, the transducers also exhibit a sensitivity to transverse temperature gradients. To evaluate the magnitude of this effect, two one-dimensional temperature distributions are compared. Figure 12 shows the thermal model and temperature distribution through the Rogers Duroid 5880 insulator and the transducer assembly. The silicon wafer reaches a temperature of 587 deg *R*

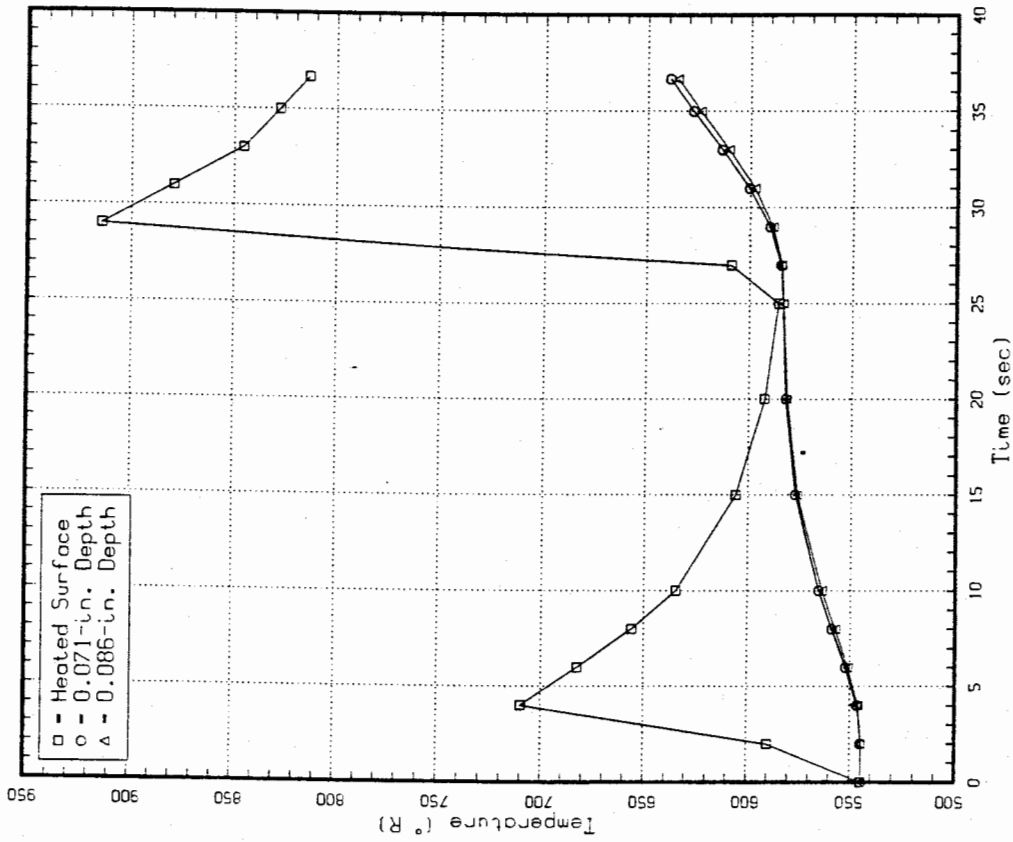
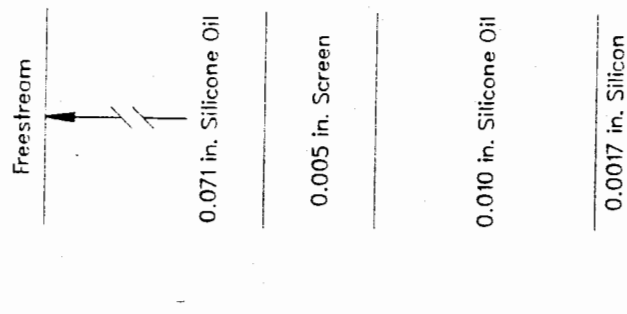


Figure 11: Thermal Model and Predicted Pressure Transducer Temperature Beneath a Cavity Filled with Silicone Oil

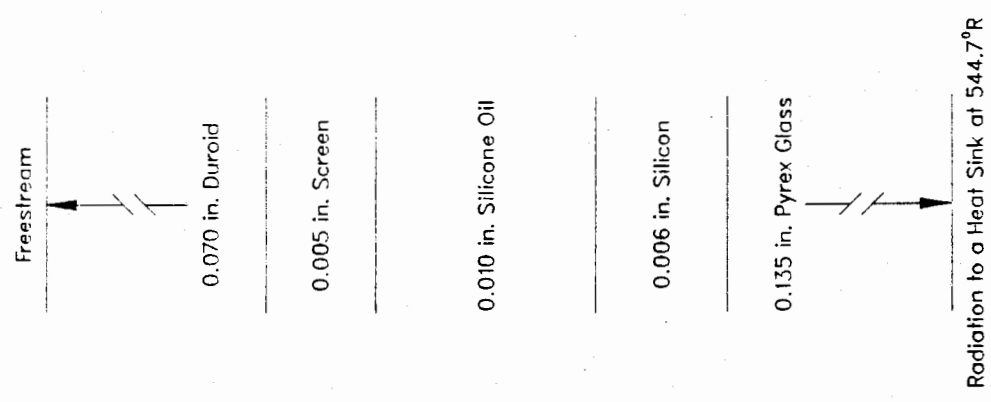
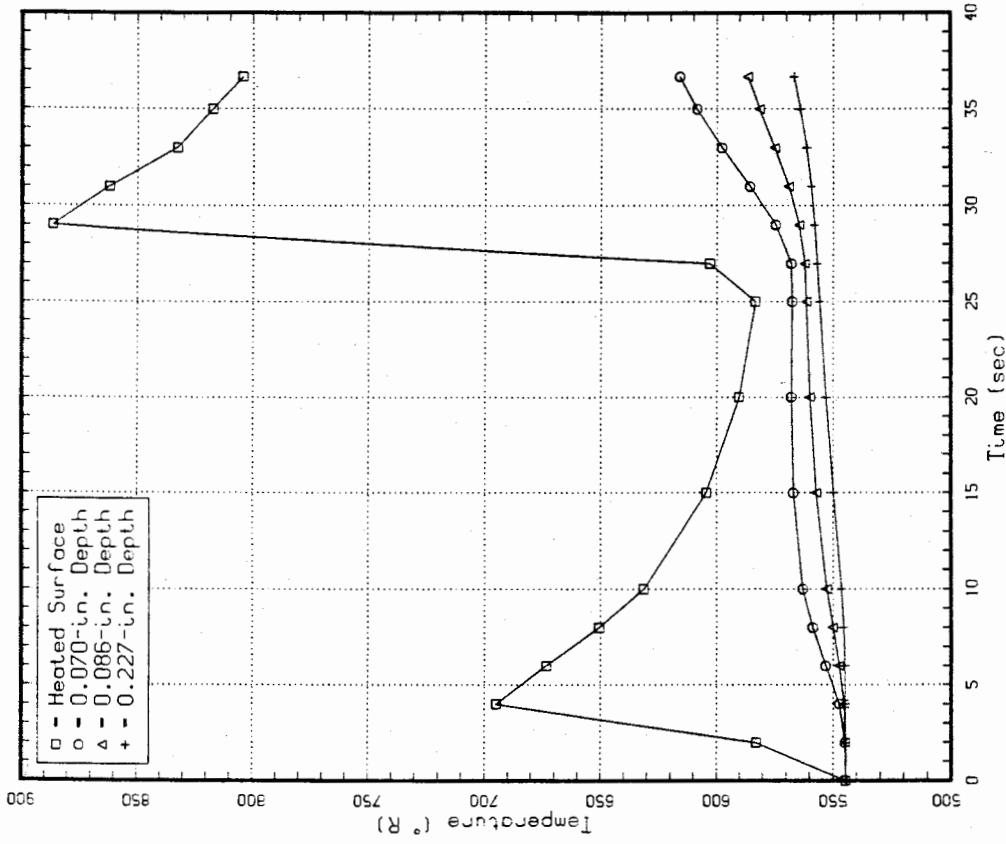


Figure 12: Thermal Model and Predicted Pressure Transducer Temperature Beneath a Duroid Washer

beneath the insulating washer. As shown earlier in Figure 11, the silicon wafer reaches a temperature of 636 deg R beneath the cavity filled with silicone oil. The difference between these temperatures sets an upper bound of 49 deg R on the temperature difference between the center of the silicon wafer and the edge of the wafer. In reality, two-dimensional heat transfer effects will reduce this difference.

7 Heat Transfer to the Bottom of a Cavity

Very few experimental measurements of heat transfer to the bottom of a cavity and only crude theoretical analyses of the problem exist. The heat transfer to the bottom of a cavity depends on the state of the boundary layer, either laminar or turbulent, the cavity length in the flow direction, L , the cavity depth, H , boundary layer edge conditions, and any interaction between these variables. In addition, most previous research concentrated on understanding and quantifying the increase in heat transfer rates caused by reattachment of a cavity free shear layer rather than the attenuation of heat transfer at the bottom of a cavity. References [1,2,7] review the available literature on heat transfer in separated flows. Most investigators studied two-dimensional channels or rectangular notches. In order to estimate the cavity size needed to protect the ASP pressure transducers, two-dimensional results are used to estimate the heat transfer at the bottom of a round hole. In [5], Nestler justified a two-dimensional analysis of measurements taken in round holes as representative of a slice through the middle of the holes.

The literature makes the distinction between a cavity and a gap. A cavity is large in the flow direction relative to the boundary layer thickness of the external flow. The ratio of cavity length to boundary layer thickness, L/δ , is much greater than 1. This feature allows simpler experimental setups because the apparatus can be of reasonable size. On the other hand, a gap has a value of L/δ less than or equal to 1. Not only does this complicate any theoretical analysis, it also means that the dimensions of any experimental investigation must be small and measurement uncertainty large. As noted before, the minimum ASP cavity diameter is 0.050 in. The GE reentry vehicle heating program [9] predicts a turbulent boundary layer thickness of 0.164 in. at the 27.33-in. station for a freestream Mach number of 1.8 and an altitude of 0.0 ft. This yields a L/δ ratio of 0.30. The ASP cavity, therefore, falls in the gap regime.

Most theoretical analyses or correlations of heat transfer to cavities and gaps, under either laminar or turbulent boundary layers, begin with calculation of the heat addition to the recirculating region. The heat addition is given by:

$$q_c = \frac{1}{L} \int_0^L \left[k_d \frac{\partial T}{\partial y} + u_d \mu_d \frac{\partial u}{\partial y} \right] dx \quad (1)$$

where

k_d = thermal conductivity of air along the dividing streamline

the measured heat flux ratios on the upstream and downstream sides of the gaps at a given depth could be averaged to obtain the equivalent heat flux ratio to the bottom of a gap with the same depth. Appendix B contains the data points obtained in this manner.

In Reference [8], Nestler, Saydah, and Auxer measured the heat transfer along the walls and bottoms of cavities and gaps under a turbulent boundary layer. They also developed a correlation of the heat transfer to the bottom of both cavities and gaps using the data presented in the paper and other experimental data.

$$\frac{q_b}{q_s} = 1.88 \frac{Re_s^{0.2}}{\left(1 + 2\frac{H}{L}\right) \left(1 + \frac{\gamma-1}{2} M_e^2\right) \frac{q}{q_i} \sigma} = 1.88 \Phi \quad (3)$$

where

Re_s = Reynolds number based on boundary layer edge conditions and distance from the leading edge of the flat plate.

M_e = boundary layer edge Mach number

$\frac{q}{q_i}$ = ratio of compressible to incompressible heat flux on a flat plate

σ = turbulent shear layer spread parameter, assumed to vary linearly from a value of 12 at $M = 0$, to 16 at $M = 2$ and constant thereafter, [6].

Nestler et al. developed the correlation by deriving a relationship for q_c/q_s assuming the growth of an asymptotic turbulent free shear layer over the cavity. That analysis produced

$$\frac{q_c}{q_s} \approx \frac{Re_s^{0.2}}{\left(1 + \frac{\gamma-1}{2} M_e^2\right) \frac{q}{q_i} \sigma} \quad (4)$$

They then assumed that the heat flux to the bottom of the recirculating region is proportional to the average heat flux to the walls of the recirculating region.

$$q_b \approx q_c \frac{L}{L + 2H} = q_c \frac{1}{1 + 2\frac{H}{L}} \quad (5)$$

Note that the development of the correlation does not apply to gaps because of the assumption of an asymptotic turbulent free layer growing over the cavity. Note also that the cavity or gap length has no effect on the q_c/q_s ratio. As mentioned before, q_c/q_s should go to 1 as the recirculating region length goes to 0.

Figure 13 shows the correlation plotted with the two experimental gap data points from Reference [8] and four points derived from Reference [11]. In Reference [11], Weinstein et al. did not give sufficient information to allow calculation of the boundary layer edge conditions when the flat plate model was positioned at an angle of attack. The four points plotted in Figure 13 correspond to the 0.0 degree angle of attack condition. The figure shows that the correlation, developed for cavities, does not do well in the gap regime. The correlation does, however, split the data.

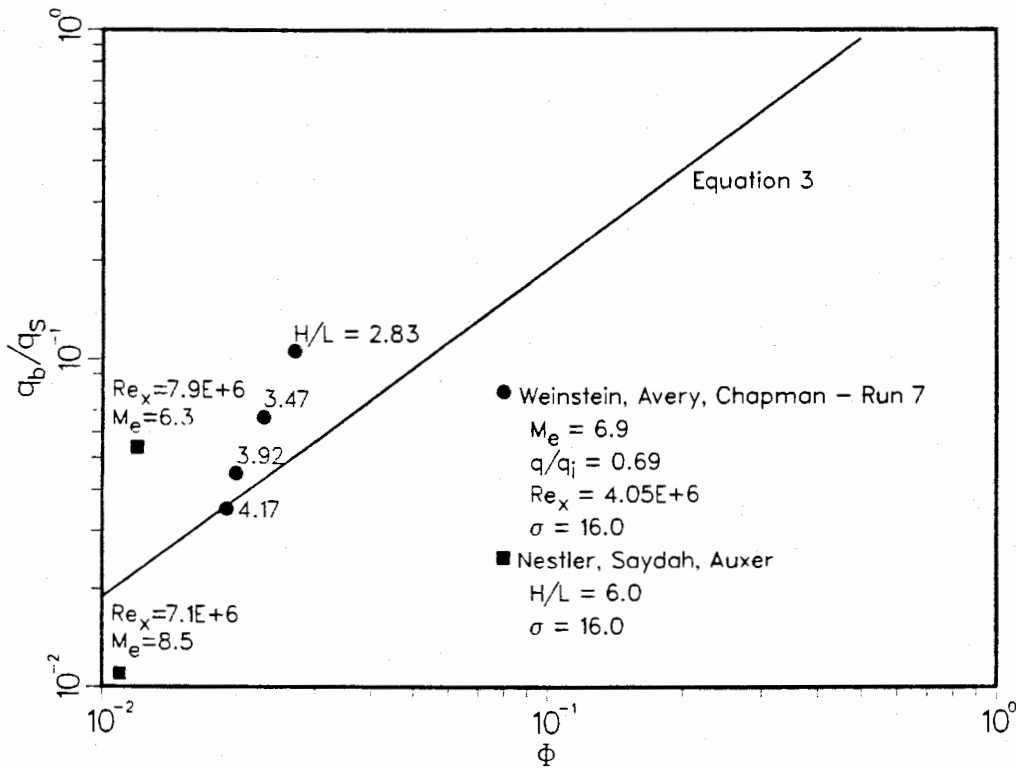


Figure 13: Nestler, Saydah, and Auxer Gap Bottom Heating Correlation

8 Conclusion

Although the aerothermal environment experienced by the ASP vehicle is mild by comparison with reentry vehicle environments, the fragile construction of the surface pressure transducers nevertheless required that they be insulated from that environment. A proposal to cover the transducers with RTV proved unacceptable because the required thick layer of RTV destroyed transducer frequency response and repeatability. Recessing the transducer below the surface also failed to provide a solution to the thermal protection problem because the required cavity depth to diameter ratio would again destroy transducer frequency response. The solution to the problem was found by recessing the pressure transducer below the surface in a shallow cavity and filling the cavity with a viscous, incompressible, silicone oil.

9 References

- [1] A. F. Charwat, *Supersonic Flows with Embedded Shock Regions*, Advances in Heat Transfer, Academic Press, 1970.
- [2] L. S. Fletcher, D. G. Briggs, and R. H. Page, *Heat Transfer in Separated and Reattached Flows*, Israel Journal of Technology, vol. 12, 1974, pp. 236-261.
- [3] L. M. Lauger, P. C. Kaestner, and B. F. Blackwell, *Operation Instructions for Charring Material Ablation Code*, SLA-73-0745, Sandia National Laboratories, Albuquerque, August, 1973, revised by S. G. Beard, December 1985.
- [4] S. McAlees, private communication, Aerothermodynamics Division 1553, Sandia National Laboratories, January, 1986.
- [5] D. E. Nestler, *Hypersonic Laminar Cavity Heat Transfer*, Proceedings of the 4th International Heat Transfer Conference, vol. 3, Versailles, September, 1970.
- [6] D. E. Nestler, *An Engineering Analysis of Reattaching Shear Layer Heat Transfer*, AIAA-72-717, June, 1972.
- [7] D. E. Nestler, *The Effects of Surface Discontinuities on Convective Heat Transfer in Hypersonic Flow*, AIAA-85-0971, June, 1985.
- [8] D. E. Nestler, A. R. Saydah, and W. L. Auxer, *Heat Transfer to Steps and Cavities in Hypersonic Turbulent Flow*, AIAA-68-673, June, 1968.
- [9] D. H. Richbourg, *A Three-Dimensional Boundary-Layer Computer Program for Sphere-Cone Type Reentry Vehicles*, Volume 2, User's Manual, AFFDL-TR-78-67, June, 1978.
- [10] A. L. Thornton, *LOVEL-84: A Low Velocity Aerodynamic Heating Code for Flat Plates, Wedges, and Cones*, SAND84-0457, Sandia National Laboratories, Albuquerque, May, 1984.
- [11] I. Weinstein, D. E. Avery, and A. J. Chapman, *Aerodynamic Heating to the Gaps and Surfaces of Simulated Reusable-Surface-Insulation Tile Arrays in Turbulent Flow at Mach 6.6*, NASA TM X-3225, November, 1975.

Appendix A
Vehicle Trajectory

Computed Atmospheric Trajectory

TIME	EL	ANG	ALT	VEL(E)	RANGE	MACH	ACC(L)	THRUST	DRAG	Q	RN/L	INST. WT
	DEG		FT	FPS	FT		FPS/S	G	G	PSF	1/FT	LB
0.00	32.500		35.0	0.0	0.0	0.00	-17.3	0.001	0.000	0.000	0.000	2761.500
.07	32.500		35.0	0.0	0.0	0.00	0.00	0.537	0.000	0.000	0.000	2761.227
.20	32.500		35.7	35.2	1.0	0.03	516.2	16.581	-0.000	1.474	224680.778	2744.298
.40	32.500		44.9	138.6	15.5	.12	525.5	16.874	-0.004	22.809	883789.687	2696.614
.60	30.807		65.1	245.6	15.7	.12	525.6	16.877	-0.004	23.075	888927.013	2696.246
.80	29.732		95.2	353.8	48.5	.22	536.0	17.184	-0.012	71.568	1565027.529	2648.193
1.00	28.941		135.3	464.1	100.3	.32	546.4	17.502	-0.024	148.434	2252889.652	2600.141
1.20	28.317		185.1	576.6	262.9	.42	556.9	17.833	-0.042	255.139	2951979.700	2552.089
1.40	27.802		244.7	691.1	374.8	.62	567.5	18.177	-0.065	393.159	3661884.021	2504.036
1.60	27.365		314.0	807.9	507.6	.72	578.3	18.535	-0.094	563.981	4382252.647	2455.984
1.80	26.986		393.2	926.8	661.9	.83	589.0	18.908	-0.140	769.045	5112555.436	2407.932
2.00	26.653		482.2	1047.5	838.1	.94	599.4	19.296	-0.213	1009.709	5852148.837	2359.879
2.20	26.355		581.2	1169.2	1036.5	1.05	602.5	20.123	-0.363	1286.593	6598665.469	2311.827
2.40	26.085		689.8	1290.1	1257.1	1.15	607.3	20.564	-0.953	1598.516	7348531.112	2263.775
2.60	25.840		808.1	1412.1	1500.0	1.26	613.7	21.026	-1.248	1939.751	8082824.842	2215.722
2.80	25.614		936.0	1535.5	1765.6	1.38	620.6	21.509	-1.517	2316.168	8821203.318	2167.670
3.00	25.406		1073.6	1660.7	2054.0	1.49	627.4	22.015	-1.789	2728.487	9562057.261	2119.618
3.20	25.212		1220.2	1758.2	2363.9	1.58	645.3	22.488	-2.085	3178.523	10307534.321	2071.565
3.40	25.024		1371.6	1799.5	2686.9	1.61	66.1	4.588	-2.329	3547.161	10875550.744	2033.124
3.50	24.932		1447.6	1798.8	2850.1	1.61	-78.9	0.074	-2.106	3699.312	11093777.246	2013.903
3.50	24.932		1447.6	1798.8	2850.1	1.61	-103.2	0.000	-2.785	3687.901	11070916.401	2011.500
3.60	24.838		1523.1	1788.5	3012.8	1.61	-101.9	0.000	-2.747	3637.773	10990128.734	1993.000
3.80	24.650		1671.9	1766.6	3335.7	1.59	-112.9	0.000	-3.093	3533.197	10821800.305	1993.000
4.00	24.459		1817.8	1744.3	3655.0	1.57	-110.3	0.000	-3.013	3429.397	10654111.500	1993.000
4.20	24.265		1960.8	1722.5	3970.8	1.55	-107.7	0.000	-2.937	3329.803	10492269.381	1993.000
4.40	24.069		2100.9	1701.2	4283.2	1.53	-105.2	0.000	-2.863	3234.442	10331346.043	1993.000
4.60	23.870		2238.3	1680.4	4592.1	1.51	-102.8	0.000	-2.792	3143.008	10172820.446	1993.000
4.80	23.668		2373.0	1660.0	4897.8	1.50	-100.5	0.000	-2.724	3055.220	10018167.971	1993.000
5.00	23.463		2504.9	1640.1	5200.3	1.48	-98.3	0.000	-2.658	2970.896	9867276.874	1993.000
5.50	22.939		2823.2	1592.3	5943.0	1.44	-93.0	0.000	-2.502	2774.134	9505806.207	1993.000
6.00	22.397		3125.7	1547.0	6667.1	1.40	-88.2	0.000	-2.360	2595.302	9166766.430	1993.000
6.50	21.837		3412.9	1504.1	7373.6	1.36	-83.6	0.000	-2.228	2432.123	8849883.496	1993.000
7.00	21.260		3685.4	1463.3	8063.5	1.33	-79.4	0.000	-2.106	2283.166	8552297.963	1993.000
7.50	20.664		3943.6	1424.6	8737.6	1.29	-75.5	0.000	-1.993	2146.934	8272545.388	1993.000
8.00	20.049		4188.2	1387.8	9396.8	1.26	-71.8	0.000	-1.889	2022.329	8010122.792	1993.000
8.50	19.416		4419.6	1352.8	10041.6	1.23	-68.4	0.000	-1.793	1908.090	7763489.282	1993.000
9.00	18.764		4638.1	1319.4	10672.8	1.20	-65.1	0.000	-1.703	1803.124	7531270.995	1993.000
9.50	18.094		4844.1	1287.7	11291.1	1.17	-61.6	0.000	-1.605	1706.895	7313227.057	1993.000
10.00	17.404		5038.1	1257.7	11897.1	1.14	-58.4	0.000	-1.515	1618.799	7108907.796	1993.000
10.50	16.696		5220.5	1229.3	12491.5	1.12	-55.3	0.000	-1.433	1537.969	6917200.651	1993.000
11.00	15.969		5391.4	1202.4	13074.8	1.10	-52.5	0.000	-1.358	1463.653	6737107.442	1993.000
11.50	15.223		5551.3	1176.7	13647.6	1.07	-49.9	0.000	-1.290	1395.200	6567750.347	1993.000
12.00	14.458		5700.5	1152.4	14210.4	1.05	-47.5	0.000	-1.227	1332.058	6408387.014	1993.000
12.50	13.675		5839.2	1130.7	14763.9	1.03	-39.1	0.000	-0.979	1277.076	6266539.266	1993.000
13.00	12.876		5968.0	1113.0	15309.7	1.02	-32.2	0.000	-0.777	1232.501	6148744.331	1993.000
13.50	12.062		6087.3	1098.3	15849.3	1.00	-26.7	0.000	-0.620	1195.904	6049905.515	1993.000

F

FM

L

BO

NP

Trajectory After Water Entry

Time (sec)	Velocity (ft/sec)	Depth (ft)	Temperature (deg R)
0.0000E+00	0.2012E+04	0.0000E+00	0.5417E+03
0.1000E+00	0.1405E+04	0.6000E+02	0.5410E+03
0.2000E+00	0.1100E+04	0.1060E+03	0.5404E+03
0.3000E+00	0.8850E+03	0.1390E+03	0.5397E+03
0.4000E+00	0.7100E+03	0.1680E+03	0.5391E+03
0.5000E+00	0.5700E+03	0.1890E+03	0.5387E+03
0.6000E+00	0.4600E+03	0.2070E+03	0.5383E+03
0.7000E+00	0.3600E+03	0.2230E+03	0.5380E+03
0.8000E+00	0.2700E+03	0.2340E+03	0.5377E+03
0.9000E+00	0.1850E+03	0.2380E+03	0.5376E+03
0.1000E+01	0.1050E+03	0.2430E+03	0.5375E+03
0.1200E+01	0.8500E+02	0.2520E+03	0.5373E+03
0.1400E+01	0.6500E+02	0.2610E+03	0.5371E+03
0.1600E+01	0.5250E+02	0.2700E+03	0.5369E+03
0.1800E+01	0.4750E+02	0.2790E+03	0.5367E+03
0.2000E+01	0.4600E+02	0.2880E+03	0.5365E+03
0.4000E+01	0.4600E+02	0.3770E+03	0.5340E+03
0.6000E+01	0.4600E+02	0.4660E+03	0.5314E+03
0.8000E+01	0.4500E+02	0.5540E+03	0.5285E+03
0.1000E+02	0.4400E+02	0.6430E+03	0.5256E+03
0.1200E+02	0.4400E+02	0.7320E+03	0.5225E+03

Appendix B

Gap Heating Data Derived From Reference 11

Run	δ^* (cm)	L (cm)	H (cm)	$\left[\frac{q}{q_{FF}}\right]_D$	$\left[\frac{q}{q_{FF}}\right]_U$	$\left[\frac{q}{q_{FF}}\right]_{avg}$
8	0.81	0.18	0.353	0.500	0.199	0.350
			0.510	0.292	0.160	0.226
			0.625	0.172	0.116	0.144
			0.750	0.097	0.094	0.096
6	1.17	0.18	0.510	0.171	0.115	0.143
			0.625	0.113	0.085	0.099
			0.750	0.066	0.063	0.065
5	1.17	0.30	0.510	0.276	0.275	0.275
			0.625	0.185	0.238	0.212
			0.750	0.111	0.212	0.162
			0.850	0.052	0.206	0.129
4	1.17	0.41	0.510	0.312	0.263	0.288
			0.625	0.229	0.222	0.226
			0.750	0.137	0.196	0.167
			1.162	0.000	0.153	0.077
7	1.62	0.18	0.510	0.148	0.064	0.106
			0.625	0.093	0.040	0.067
			0.706	0.061	0.028	0.045
			0.750	0.048	0.022	0.035

where

D = quantity measured on the downstream cavity wall

U = quantity measured on the upstream cavity wall

avg = average of the upstream and downstream wall values

Distribution

1510 J. W. Nunziato
1520 D. J. McCloskey
1530 L. W. Davison
1540 R. C. Luth
1550 R. C. Maydew
1551 J. K. Cole
1552 C. W. Peterson
1553 S. McAlees, Jr.
1553 D. N. Benton (5)
1554 D. D. McBride
1555 W. R. Barton
1556 W. L. Oberkampf
3141 S. A. Landenberger (5)
3151 W. L. Garner
8024 P. W. Dean
8150 J. B. Wright
8152 J. C. Swearngen
8152 M. T. Ferrario

